PERGAMON

International Journal of Heat and Mass Transfer 45 (2002) 1615–1629

International Journal of HEAT and MASS TRANSFER

www.elsevier.com/locate/ijhmt

An experimental and numerical study of heat transfer off an inclined surface subject to an impinging airflow

Subrata Roy [a,*], Karim Nasr [a], Paresh Patel [a], Bashar AbdulNour [b]

[a] *Mechanical Engineering Department, Kettering University, 1700 West Third Avenue, Flint, MI 48504-4898, USA*
[b] *Technology Development Department, Ford Motor Company, Dearborn, MI 48120, USA*

Received 27 December 2000; received in revised form 23 August 2001

Abstract

Understanding the heat transfer interaction between an impinging jet and an inclined surface is of paramount practical significance. In this paper, the heat transfer process is investigated utilizing a three-dimensional finite volume numerical method and renormalization group (RNG) theory based k–ε turbulence model. The issuing incompressible jet is impinging upon the inside of an inclined surface creating a thermal boundary layer and a fully three-dimensional vortex structure. Numerical analyses predict a detailed description of fluid flow patterns and heat transfer coefficients. Experimental investigations are performed on the inner surface for the purpose of obtaining local and average heat transfer coefficients and further validation of the numerical results. The effect of different turbulence levels in the numerical solution is also reported.

Keywords: Climate control; Inclined surface; Impinging jets; Rectangular slots

1. Introduction

The flow of an impinging air jet on an inclined surface addresses a number of practical applications. Industrial applications include defogging and deicing of a vehicle's windshield, vertical/short takeoff and landing (V/STOL) engineering, film cooling of turbine blades, electronics cooling, and waste disposal from smokestacks into the atmosphere. In many of these applications, the temperature distribution resulting from the jet attachment to the inclined plane, and the trajectory and the physical path of the jet are critical design parameters. In this paper, the specific application of interest is air issuing from the defroster's nozzles of a vehicle and impinging on the glass windshield. Various factors can be examined for optimizing the flow performance for defrosting ice on the outside surface or clearing fog on the inside surface. The nozzle outlet must be capable of generating an airflow that disperses over the entire inner surface of the windshield. Extensive testing on vehicle systems and components would generally meet specific customer requirements. However, utilizing Computational Fluid Dynamics (CFD) tools, a designer can predict the performance of a system and optimize its objectives cost-effectively by complementing numerical computation with fewer experiments.

Fig. 1 describes the schematic of a vehicle windshield and its associated air volume. The air jet at temperature T_j is issued at an angle ϕ through two rectangular slots (openings), and impinges upon the glass (inclined surface). The windshield of thickness t, width H and length L is inclined at an angle α. All necessary dimensions are given in Fig. 1. A heating pad is centrally placed on the external surface of the windshield. The heating pad introduces a constant heat flux into the heated area. The mean flow velocities in the driver and passenger side openings are V_d and V_p, respectively.

The interaction of multiple cool air jets with a hot inclined wall generates a complex flow field that has been extensively investigated in the literature. A number of investigators had tackled the *specific* problem of air

* Corresponding author. Tel.: +1-810-762-9949; fax: +1-810-762-7860.

E-mail addresses: sroy@kettering.edu (S. Roy), knasr@kettering.edu (K. Nasr), ppatel@kettering.edu (P. Patel), babdulno@ford.com (B. AbdulNour).

0017-9310/02/$ - see front matter
PII: S0017-9310(01)00276-9

Nomenclature

a	coefficient in discretized equation
$\mathbf{B}, \mathbf{b}$	source terms in discretized equation
d	minor axis of the hole cross-section
D	major axis of the hole cross-section
$\mathbf{f}$	flux term
G	generation of turbulence term
$g^{\xi_i \xi_j}$	contravariant metric
h	convective heat transfer coefficient
Ja	Jacobian of the transformation
k	turbulent kinetic energy
p	pressure
$\mathbf{q}$	vector of unknowns
R	flow ratio
$\mathbf{S}$	source term in Navier–Stokes equations
u_i	Cartesian velocity component
U^{ξ_i}	contravariant velocity component
U_0	freestream fluid velocity
x_i	Cartesian coordinate
y^+	inner variable, $u_\tau y/v$

Greek symbols

ε	dissipation rate of turbulent kinetic energy
Γ	diffusion coefficient
β	coefficient of thermal expansion
μ	viscosity
ρ	density
ξ_i	coordinate in the transformed space
α	jet issuing angle

Subscripts

eff	effective
e, w	east, west
n, s	north, south
f, r	front, rear
v	viscous term
x_i	partial derivative in the physical space
ξ_i	partial derivative in the computational space

issuing from the defroster's nozzles and impinging on the inclined surface of a vehicle's windshield. The main objective of these investigations was to enhance the defroster's performance in providing clear areas free of frost or fog. Some investigators have addressed the airflow distribution [1,2], while others have utilized infrared (IR) thermal imaging (or thermography) for measurements of thermal patterns [3,4]). The IR imaging system is non-intrusive, measuring local surface temperatures with a real time response but at a higher cost than other techniques for temperature measurement.

The actual flow exiting the defroster's nozzles possesses a number of complexities making the numerical solution quite a challenge. Some of these complexities are that the issuing jets are rectangular, obliquely impinging, turbulent with non-uniform (hydrodynamically and thermally) exit conditions. Willenborg et al. [5] have documented defroster flow measurement details, where hot-wire velocity measurements in the defroster nozzle jet flow and in the immediate vicinity of the windshield interior surface were performed. Another experimental study [6] had been conducted to establish the parameters influencing the convection heat transfer coefficient h on the windshield. As a result, a two-dimensional wall jet for isothermal and uniform heat flux boundary conditions was determined experimentally using hot-wire, micro thermocouples, and thermal imaging surveys. The local value of h was found to be insensitive to the thermal boundary condition, especially in the turbulent downstream region. A recent survey of relevant investigations [7] point to the heat transfer coefficient being the primary controlling parameter whose quantification is desired and yet to be achieved.

Although extensive experimental studies have been conducted on this application, reliable flow and thermal measurements remain expensive and are limited by the amount of data that can be collected. Ikeda et al. [8] presented the results of experimental and CFD analyses of airflow distribution on inclined surfaces from defroster nozzles. Their CFD analysis employed an unstructured grid of a commercial code for the comparison of experimental and computational results. Sugano et al. [9] documented a numerical method for predicting the defroster cleaning pattern using three-dimensional airflow analysis that showed good agreement with experimental observations. AbdulNour and Foss [10], and Brewster et al. [11] concluded that numerical simulation of defroster and windshield airflow is a valid technique for gaining valuable insight into the flow field, both in direction and in magnitude.

There is also ample published literature on the *general* issue of jet impingement heat transfer on a surface. The majority of these studies focus on the theoretical treatment of the problem by modeling (numerically) or experimenting with laboratory-controlled systems using axisymmetric jets impinging on flat plates. Polat et al. [12] presented a relatively recent review of numerical studies related to impinging jets. An experimental study on incompressible jets issuing into a cross-flow was reported by Andreopoulos and Rodi [13]. More reviews were also documented by Martin [14], Downs and James [15], and Viskanta [16].

In the present paper, the fluid-thermal characteristics of an impinging jet on an inclined surface are identified. Experimental measurements of local surface temperatures, using liquid crystals, and similar to the technique performed by Simonich and Moffat [17], yielded local

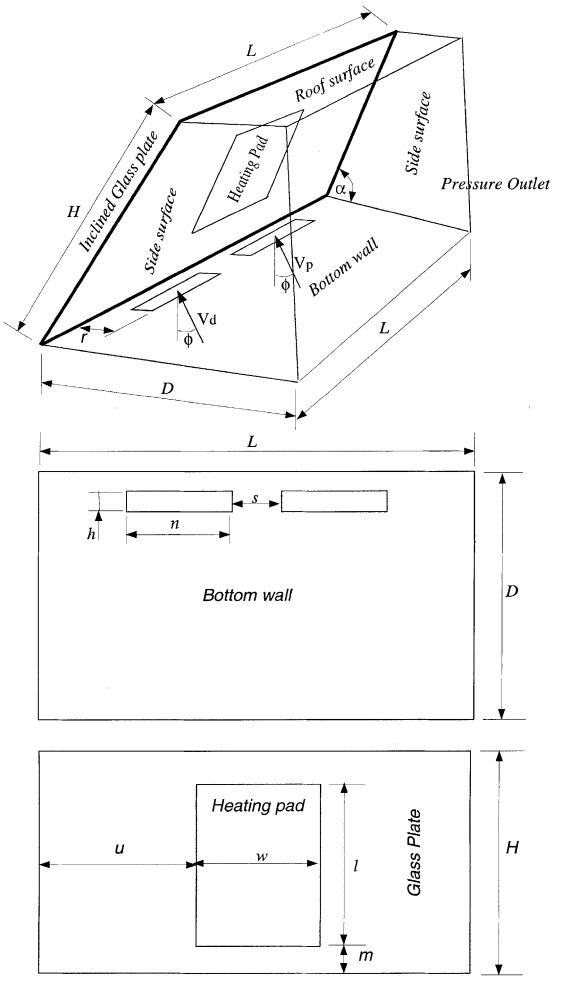

Fig. 1. Schematic drawing of the simulation domain.

heat transfer coefficients for an imposed heat flux. A map of heat transfer coefficients between the surface and the incoming jet is obtained. A corresponding three-dimensional computational model is generated by Hypermesh [18] grid generation software. The temperature and flow distributions details are obtained by numerical simulation using FLUENT [19] finite volume commercial code. The effect of three different inlet turbulence levels is also reported. Finally, the numerical solution is validated with experimental data and the predicted local and average heat transfer coefficients are compared to the experimentally based values.

2. Theoretical formulation

2.1. Governing equations

The system of equations for steady, turbulent, buoyancy-driven, incompressible jet flows, including the k–ε model has been studied in detail in the literature [20]. For state variable $\mathbf{q} = [1\ u\ v\ w\ k\ \varepsilon\ T]^{\mathrm{T}}$, the transformed equations for the intrinsic coordinate system ξ_i can be written as [21]

$$\frac{\partial \mathbf{f}^{\xi_i}}{\partial \xi_i} = \frac{\partial}{\partial \xi_i}\left(\mathbf{f}_v^{\xi_i} + \hat{\mathbf{f}}_v^{\xi_i}\right) + \mathbf{S}, \tag{1}$$

where $\mathbf{S}$ is the source term which includes Boussinesq approximation for the momentum equation, $\mathbf{f}^{\xi_i}$ is the convective flux vector, and $\mathbf{f}_v^{\xi_i}$ and $\hat{\mathbf{f}}_v^{\xi_i}$ are the diffusive flux vectors, given by

$$\mathbf{f}^{\xi_i} \equiv \rho U^{\xi_i}\mathbf{q}, \quad \mathbf{f}_v^{\xi_i} = \Gamma_{\mathrm{eff}} g^{\xi_i\xi_i}\frac{\partial \mathbf{q}}{\partial \xi_i}, \quad \text{and}$$

$$\hat{\mathbf{f}}_v^{\xi_i} = \Gamma_{\mathrm{eff}} g^{\xi_i\xi_j}\frac{\partial \mathbf{q}}{\partial \xi_j}, \quad i \neq j. \tag{2}$$

In the above equations U^{ξ_i} is the scaled ξ_i component of the contravariant velocity vector, and $g^{\xi_i\xi_j}$ are metric components introduced from the transformation of the equations from the physical (x_i: x, y, z) to the computational (ξ_i: ξ, η, ζ) space

$$U^{\xi_i} = Ja\left(u_j\frac{\partial \xi_i}{\partial x_i}\right) \quad \text{and} \quad g^{\xi_i\xi_j} = Ja\left(\frac{\partial \xi_i}{\partial x_k}\frac{\partial \xi_j}{\partial x_k}\right), \tag{3}$$

where Ja is the Jacobian of the transformation matrix.

2.2. Turbulence modeling

In this work, a renormalization group (RNG) based k–ε model of Yakhot and Orszag [22] is utilized. This model introduces two equations, one for the turbulent kinetic energy k and the other for its dissipation rate ε. These equations are included in the set of the transformed equations (1). The effect of this model is to introduce an additional viscosity, called turbulent viscosity, which is calculated as a function of density ρ by

$$\mu = C_\mu \rho \frac{k^2}{\varepsilon}, \tag{4}$$

where $C_\mu = 0.0845$ [23]. The turbulent viscosity is not a fluid property, but rather a property of the flow field. Its value is added to the molecular viscosity and yields an effective viscosity, μ_{eff}, which is used in the computational model. The k and ε at the inlet are calculated from the following expressions:

$$k_{\mathrm{in}} = \frac{3}{2}(T_u u)^2, \quad \varepsilon_{\mathrm{in}} = \frac{k_{\mathrm{in}}^{3/2}}{L_\varepsilon}, \tag{5}$$

where T_u is the turbulence level and L_ε is a characteristic length of the domain.

2.3. Discretization

Integrating (1) over a finite control volume in the computational space, the discretized form of (1) is represented as

$$\left(\tilde{\mathbf{f}}_{\mathrm{w}}^{\xi}-\tilde{\mathbf{f}}_{\mathrm{e}}^{\xi}\right)+\left(\tilde{\mathbf{f}}_{\mathrm{n}}^{\eta}-\tilde{\mathbf{f}}_{\mathrm{s}}^{\eta}\right)+\left(\tilde{\mathbf{f}}_{\mathrm{f}}^{\zeta}-\tilde{\mathbf{f}}_{\mathrm{r}}^{\zeta}\right)=\mathbf{B}\Delta\xi\Delta\eta\Delta\zeta, \tag{6}$$

where the tildas denote convective and diffusive terms, the latter are without the cross-derivative terms. The viscous terms due to the non-orthogonality of the grid (i.e., the cross-derivative terms) are grouped together into a separate source term **B**, which also includes the pressure terms and any other source terms. The convection–diffusion terms are discretized such that

$$\begin{aligned}\left(\tilde{\mathbf{f}}^{\xi_i}\right)_{\mathrm{cf}} &= \left(\mathbf{f}^{\xi_i}\right)_{\mathrm{cf}}+\left(\mathbf{f}_{v}^{\xi_i}\right)_{\mathrm{cf}}\\ &= \rho\left(U^{\xi_i}\right)_{\mathrm{cf}}\begin{bmatrix}1\\u\\v\\w\\k\\\varepsilon\\T\end{bmatrix}_{\mathrm{cf}}-\Gamma_{\mathrm{eff}}\left(g^{\xi_i\xi_i}\right)_{\mathrm{cf}}\frac{\partial}{\partial\xi_i}\begin{bmatrix}0\\u\\v\\w\\k\\\varepsilon\\T\end{bmatrix}_{\mathrm{cf}},\end{aligned} \tag{7}$$

where cf stands for cell face. The vector of unknowns at a cell face is calculated using the simple upwind scheme. In the simple upwind scheme, the value of the velocity at a cell face assumes the value of the velocity of the node in the upwind direction. Grouping the various terms together we obtain a system of equations of the following format:

$$a_P\mathbf{q}_P=a_{\mathrm{e}}\mathbf{q}_{\mathrm{e}}+a_{\mathrm{w}}\mathbf{q}_{\mathrm{w}}+a_{\mathrm{n}}\mathbf{q}_{\mathrm{n}}+a_{\mathrm{s}}\mathbf{q}_{\mathrm{s}}+a_{\mathrm{f}}\mathbf{q}_{\mathrm{f}}+a_{\mathrm{r}}\mathbf{q}_{\mathrm{r}}+\mathbf{b}, \tag{8}$$

where **b** is the source term vector, consisting of the pressure terms, the diffusion terms due to grid non-orthogonality, and the antidiffussive terms.

2.4. Solution procedure

Eqs. (1) and (2) constitute a system of non-linear algebraic equations. The system is linearized by relaxation. A streamline upwinding technique is employed for stabilizing numerical iterations. The pressure corrections are used to correct the pressure and the velocities. This predictor–corrector procedure constitutes one iteration. The solution is declared convergent when the maximum residual for each of the state variable becomes smaller than a convergence criterion of $\in$. Here, the convergence of a solution vector $\mathbf{U}\subset\mathbf{q}$ on node n is defined as the norm

$$\frac{\|\mathbf{U}_n-\mathbf{U}_{n-1}\|}{\|\mathbf{U}_n\|}\leqslant\in. \tag{9}$$

We selected $\in=10^{-3}$ for continuity, momentum, turbulence kinetic energy and its dissipation rate equations and $\in=10^{-6}$ for the energy equation.

2.5. Boundary conditions

In Fig. 1, typical wall boundary conditions, i.e., the no-slip condition for the velocities and the wall functions for k and ε, are used on the bottom surface of the control volume and on the inside of the windshield. Uniform axial velocity profiles V_{d} and V_{p} are prescribed over the driver side and passenger side openings, respectively. The k and ε are prescribed at the inlets by (5). The temperature of the jets is prescribed and a constant heat flux is applied through the heating pad. Finally, the zero gradient downstream conditions for all state variables

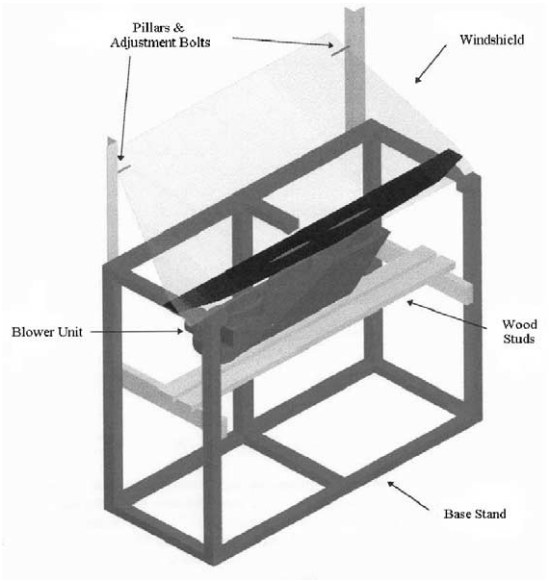

Fig. 2. A general schematic of the experimental apparatus.

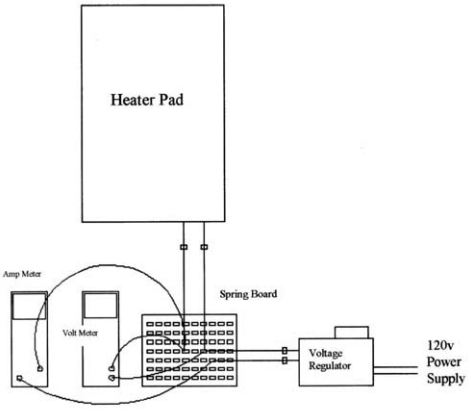

Fig. 3. Electrical wiring for the measurement of voltage and current.

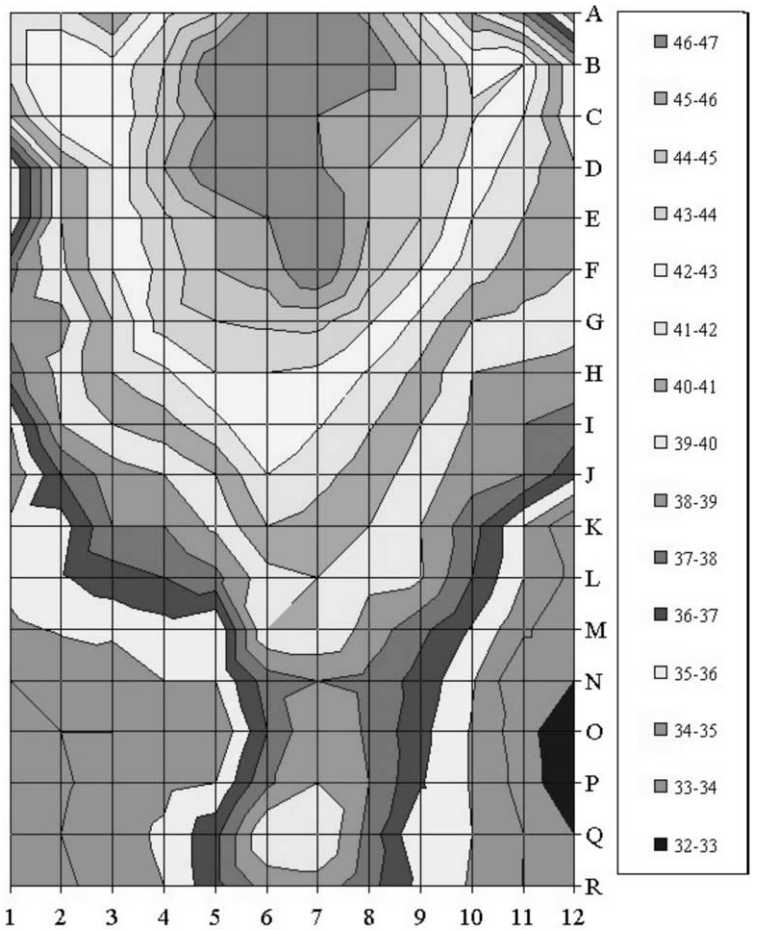

Fig. 4. Experimentally based temperature contours underneath the heated area on the inclined plate.

Table 1
Calculated heat transfer coefficients based on local temperature values (W/m^2 K)

	1	2	3	4	5	6	7	8	9	10	11	12
A			25.4		19.9	17.1	17.1		21	25.4	29.4	43.3
B		21		19.9	17.1			17.1	18.9		21	27.3
C	25.4	21	22.3		17.9			18.9	18.9		22.3	27.3
D	38.7		22.3	18.9	17.1				19.9			
E	38.7	25.4	22.3		18.9		17.1	18.9	19.9	22.3		25.4
F			22.3		18.9		17.1		21			
G			23.7		19.9					25.4		
H			23.7		21	21				27.3		
I	38.7	27.3	25.4			21					29.4	
J	43.3			27.3	25.4	22.3					29.4	
K			29.4	29.4		23.7		25.4	27.3		38.7	49.1
L				32			25.4			32	38.7	
M					38.7	25.4	25.4					49.1
N			43.3	38.7	38.7		29.4				49.1	49.1
O	49.1	43.3	43.3		43.3		27.3					56.6
P					38.7		27.3	29.4				56.6
Q		43.3				25.4	25.4		38.7	38.7	43.3	
R	49.1			38.7								49.1

are imposed on the side and roof surfaces and at the pressure outlet.

3. Results and discussion

This section is divided into two parts: the experimental results, and the numerical predictions.

3.1. Experimental results

An experimental apparatus consisting of the HVAC module of a car and a windshield was assembled. A general schematic of the experimental apparatus is shown in Fig. 2 (color figures for this paper are available at http://meweb.kettering.edu/publications/sroy/ijhmt1.pdf). Air is forced onto the inclined surface (windshield), via the blower of the HVAC module, impinges on the windshield, hugs the large surface of the windshield, and disperses into the laboratory environment. The main base of the test stand is intentionally kept open for unrestricted placement, adjustment, and accessibility of the HVAC module components. To allow for the possible adjustment of the windshield's angle between the windshield and dashpad, two pillars made of 3.81 cm perforated angle were affixed to the stand.

A representative windshield angle of a passenger vehicle was chosen as 39°, which is the angle used for the experiments. A pair of 12.7 cm bolts was placed in the appropriate pillar holes to support the windshield at the desired angle. Next, to power the blower of the HVAC module, a 12 V AC–DC power converter was chosen, wired into the blower unit and tested. A thin heating pad, 0.3048 m wide and 0.4572 m long, was attached centrally to the outer surface of the windshield providing constant surface heat flux in that region. It should be noted that in the actual application, the air is heated via a heater core and impinges on the windshield. In the current experiment, unheated room-air impinges on a heated windshield. The windshield is heated partially on its outer surface via a thermal heating pad, as mentioned earlier. The heater is capable of producing approximately 540 W. The back surface of the heating pad is insulated via a polystyrene insulation layer of known R-value. A variable resistor potentiometer was used in conjunction with two Digital Multi-Meters (DMMs) for the purpose of controlling the heat flux as shown in Fig. 3. One DMM was used to measure the voltage while the other yielded the current. Of course, the heating pad wattage (input) is the product of volts times amps. The convected heat by the flowing air is computed by: $Q_{\text{conv}} = Q_{\text{input}} - Q_{\text{loss}} - Q_{\text{rad}}$, where Q_{loss} is the rate of heat transfer, in watts, off the back surface of the heater. This heat loss was quantified based on the temperature of the back surface of the heater and the temperature of the outer surface of the insulation pad. Q_{rad} is the radiative heat transfer exchanged between the inner surface of the windshield and the surroundings, $Q_{\text{rad}} = \varepsilon\sigma A(T_s^4 - T_{\text{surr}}^4)$.

The experiment was performed at a fixed blower setting and the heating pad power value was specified as

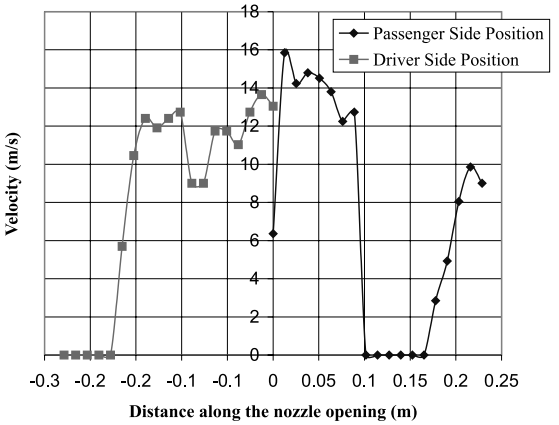

Fig. 5. Measured velocity profile along the defroster's nozzles.

Table 2
Material properties used in the numerical simulation

	Air	Glass
Density (kg/m^3)	1.225	2500
Specific heat (J/kg K)	1006.43	750
Thermal conductivity (W/m K)	0.0242	1.4
Viscosity (kg/m s)	1.7894e − 5	

Table 3
Prescribed boundary conditions (Ref. Fig. 1)

Boundary	u	v	w	T	p_{gage}	k	ε
Inclined plane	0	0	0	$\partial T/\partial\eta = 0$	$\partial p/\partial\eta = 0$	$\partial k/\partial\eta = 0$	ε_w
Heating pad	0	0	0	$Q_{\text{conv}}/A = 368$ W/m^2	$\partial p/\partial\eta = 0$	$\partial k/\partial\eta = 0$	ε_w
Inlets	Prescribed	plug flow	0	298.5 K	$\partial p/\partial\eta = 0$	k_{in}	ε_{in}
Sides	$\partial u/\partial\hat{s} = 0$	$\partial v/\partial\hat{s} = 0$	$\partial w/\partial\hat{s} = 0$	$\partial T/\partial\hat{s} = 0$	$\partial p/\partial\hat{s} = 0$	$\partial k/\partial\hat{s} = 0$	$\partial\varepsilon/\partial\hat{s} = 0$
Top	$\partial u/\partial\hat{s} = 0$	$\partial v/\partial\hat{s} = 0$	$\partial w/\partial\hat{s} = 0$	$\partial T/\partial\hat{s} = 0$	$\partial p/\partial\hat{s} = 0$	$\partial k/\partial\hat{s} = 0$	$\partial\varepsilon/\partial\hat{s} = 0$
Bottom	0	0	0	$\partial T/\partial\eta = 0$	$\partial p/\partial\eta = 0$	$\partial k/\partial\eta = 0$	ε_w

η: normal to the plane; $\hat{s}$: tangential direction(s).

$Q_{\text{input}} = 67.5$ W. For this power input, the heat flux $Q_{\text{input}}/A = 484.4$ W/m^2. The heat flux loss through the insulation pad was calculated to be $Q_{\text{loss}}/A = 29.43$ W/m^2 and the net radiative flux off the inner surface of the windshield was computed to be $Q_{\text{rad}}/A = 87$ W/m^2. Therefore, the convective flux to the flowing air was found to be $Q_{\text{conv}}/A = 368$ W/m^2. Newton's law of cooling was employed to evaluate the local heat transfer coefficients

$$h = \frac{Q_{\text{conv}}}{A(T_s - T_{\text{in}})}. \tag{10}$$

The incoming air temperature was recorded as $T_{\text{in}} = 25.5$ °C by placing a type T thermocouple at the outlet of the blower ductwork, i.e., at the defroster's nozzle exit plane. The local surface temperature of the windshield was measured by mapping the heated area of the windshield with strips of liquid crystals. These strips were placed on the inner surface of the windshield at various locations to provide a means to measure the temperature at specific locations. One hundred strips were used to capture an equivalent number of local temperatures. A grid was formed on the windshield under the entire surface of the heating pad by drawing horizontal and vertical lines with 2.54 cm spacing. This grid was used to record local points at which the inner surface temperatures are taken. The liquid crystal thermometers are strips of black plastic with adhesive on one side. Embedded in the plastic are pieces of liquid crystal temperature sensing strips. Each piece of liquid crystal has a temperature that it is sensitive too. When subjected to this temperature, it turns from black to another color. The color depends on how close to the designated temperature the strip is. For example, if the strip is exactly at the temperature, it turns green. When near the temperature but not at it, the strips turn blue or light red. Using these strips of liquid crystals, 100 local surface temperature values were recorded across the heated area. As a result, a map of local surface temperatures was generated. Fig. 4 displays an Excel-generated map (contours) of temperature values. The local surface temperature gives a local heat transfer coefficient via (10). Therefore, a map of local heat transfer coefficients can be generated as shown in Table 1.

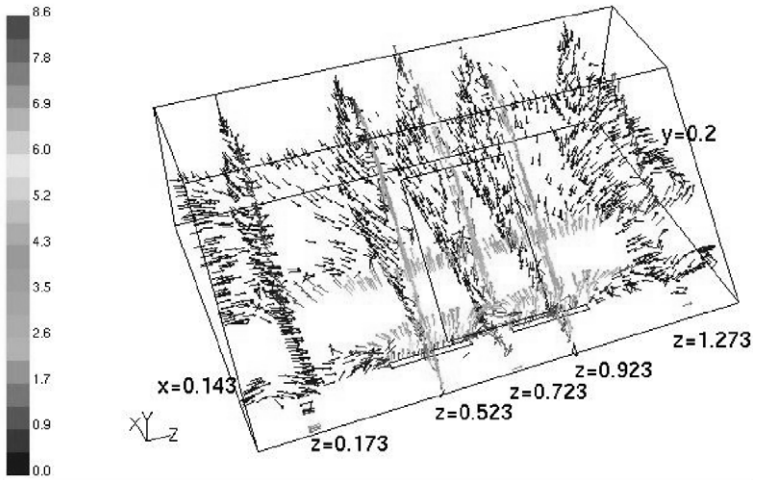

Fig. 6. Velocity distribution at different x-, y- and z-locations capturing details of the flow field.

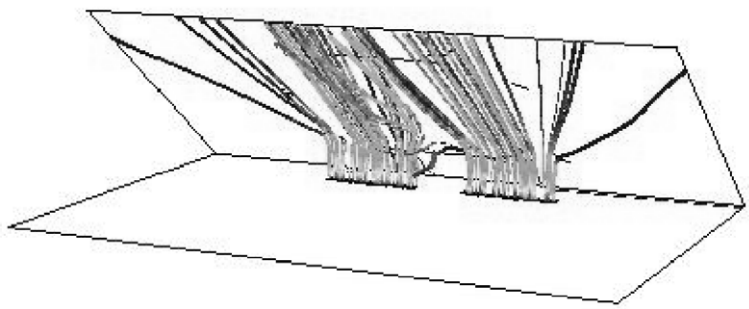

Fig. 7. Particles tracking colored by speed showing full three-dimensionality of the flow field.

Errors in computing the value of the heat transfer coefficient could result from the measurement of the voltage, the current, the heat losses, the surface area, the surface temperature, and the incoming jet air temperature. Performing an uncertainty analysis using the root-sum-square method of Moffat [24] and computing

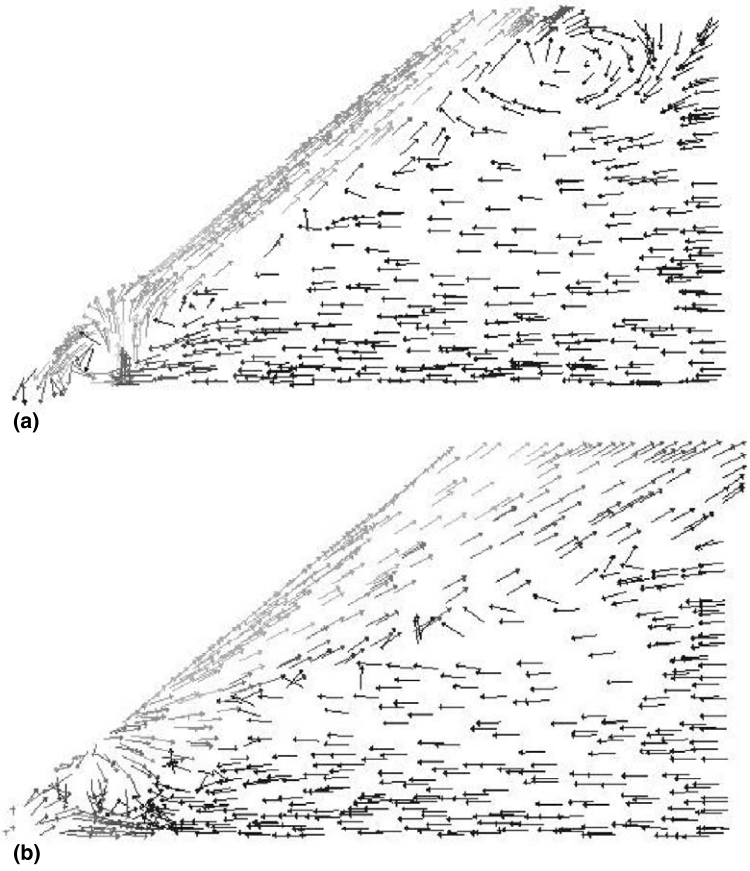

Fig. 8. Two-dimensional cross-sections show flow details at different locations across the computational domain: (a) $z = 0.5233$ m; (b) $z = 0.7233$ m.

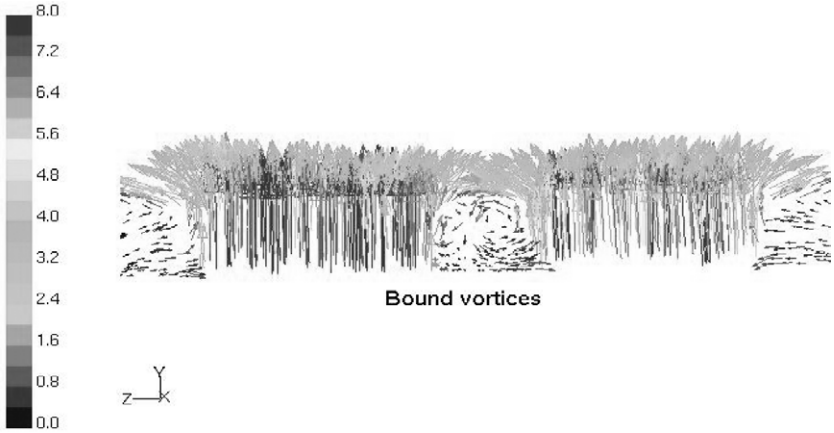

Fig. 9. Velocity vector distribution on the plane cutting through the defroster ($x = 0.144$ m) shows bound vortices in the internal region between jets.

individual relative uncertainties yielded a 5.1% relative uncertainty in the value for the heat transfer coefficient.

An average heat transfer coefficient can also be defined as:

$$\overline{h} = \frac{1}{A}\int h \, \mathrm{d}A. \tag{11}$$

The average experimentally based heat transfer coefficient over the heated area of the windshield was then computed via (11) and found to be 29.4 $\mathrm{W/m^2\,K}$. The numerical simulation discussed in the next section, compares local temperatures as well as experimental and numerical heat transfer coefficients.

It should also be noted that the velocity profile of the air blowing out of the duct onto the windshield was measured. A pitot tube attached to a manometer and placed normal to the airflow at the exit plane of the defroster's nozzle was used. Fig. 5 exhibits the non-uniform features of the velocity issuing from the defroster's nozzles for both the driver's side (left) and passenger's side (right).

3.2. Numerical predictions

The schematic of the simulation volume was shown in Fig. 1. A vertical ($\phi = 0°$) cool jet at uniform tem-

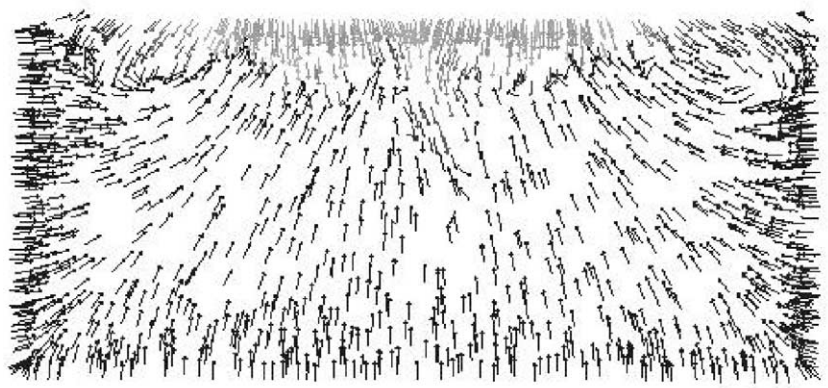

Fig. 10. Velocity vectors plotted on uniform length scale on the plane cutting through ($y = 0.2$ m) shows multiple vortex structures.

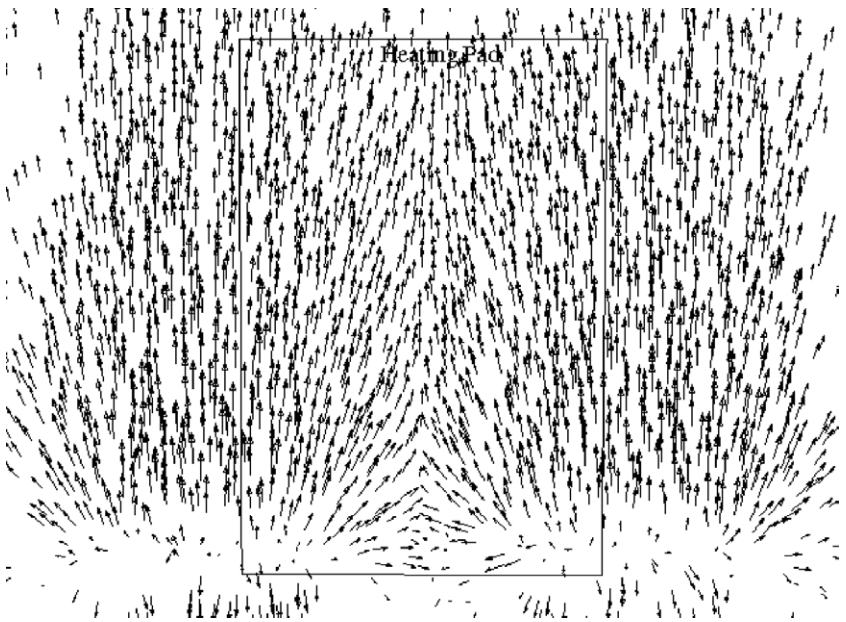

Fig. 11. Velocity distribution near the heating pad at $y^+ = 3$ on the inside surface of the windshield.

perature $T_j = 25.5\ ^\circ\mathrm{C} = 298.5$ K is impinging upon the windshield of thickness $t = 0.006$ m inclined an angle $\alpha = 39^\circ$. The injection ducts are rectangular slots with $n = 0.241$ m and $h = 0.019$ m. The distance between the slot centers $s = 0.127$ m. The geometric dimensions of the windshield and its layout match exactly those set-ups experimentally. The heating pad for the numerical simulation is bounded by $l = 0.457$ m in the longitudinal direction and $w = 0.305$ m in the lateral direction. A uniform heat flux of 368 $\mathrm{W/m^2}$ is applied on this area of the windshield. The inlet section is located at $r = 0.134$ m and the exit at $D = 0.896$ m. The other dimensions as shown in Fig. 1 are: $L = 1.447$ m, $H = 0.719$ m, $u = 0.569$ m, and $m = 0.131$ m. Despite the symmetry of the geometric configuration, the entire domain is considered for analysis due to unequal velocities at the driver and passenger sides. The material properties of air and windshield glass are shown in Table 2.

Table 3 shows the boundary conditions applied for this study. A computational mesh of 127,156 tetrahedral finite volumes was created using commercial Hypermesh software [18]. The maximum distance between the wall and the first grid point varies between $y^+ = 2.5$ for the windshield to $y^+ = 15$ for the coarsest mesh. It should be noted that factors such as mesh density, cell geometry, turbulence model, degree of approximation of the describing equations, error criterion for convergence, and numerical control parameters, could affect the speed and accuracy of the numerical solution. There are two features in the numerical model that approximate the experimental setup. The nozzles were modeled as rectangular slots, but have rounded corners in an actual HVAC module. Also, the velocity field at the exit plane of the defroster's nozzle is highly non-uniform as was shown in Fig. 5. The numerical simulation assumes uniform velocities V_d and V_p equivalent to the average value of the experimentally measured profile at the driver and passenger side, respectively.

The three-dimensional Navier–Stokes equations are solved for this fluid-thermal system using a finite volume commercial code, FLUENT [19]. The CFD solutions are documented for three different inlet turbulence levels of 10%, 5% and 2%, i.e., $T_u = 0.1, 0.05, 0.02$, respectively in (5). Figs. 6–15 plot results using $T_u = 0.1$ in (5). Fig. 6 is a three-dimensional view of the airflow characteristics inside the computational domain showing outlines of the

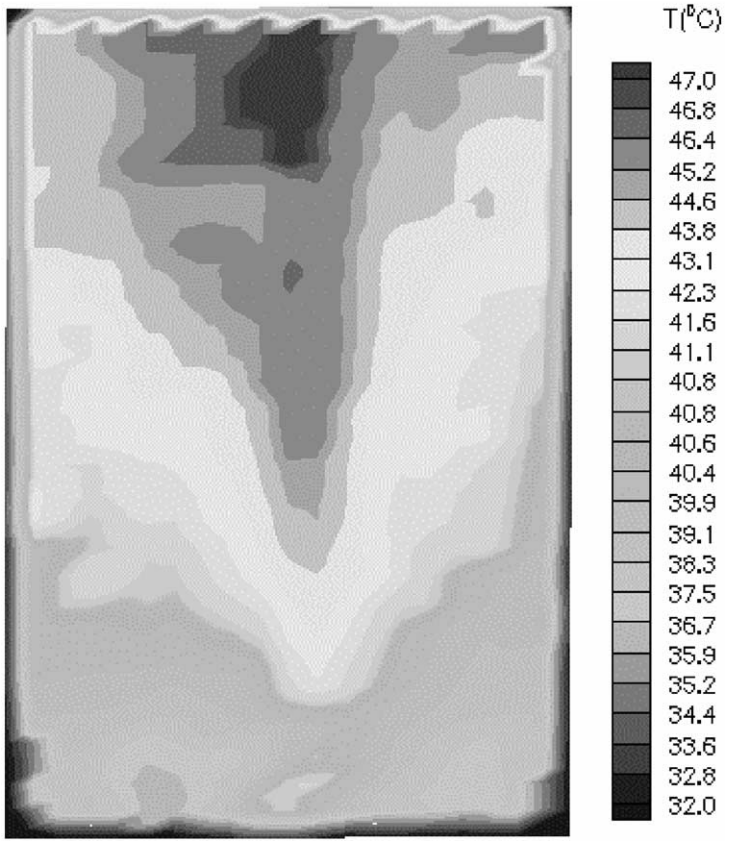

Fig. 12. Temperature distribution on the inside surface of the windshield across the heating pad.

inclined windshield, the heating pad, the inlets (defroster's nozzles), and the sidewalls. Five *xy*-planes ($z = 0.173$, 0.523, 0.723, 0.923, and 1.273 m), one *yz*-plane ($x = 0.143$ m) and one *xz*-plane ($y = 0.2$ m) document the distribution of speed inside the simulation volume. Tracking 12 particles released from each inlet in Fig. 7 shows the three-dimensional pathlines of fluid flow. The pathlines are colored by the speed of the particle.

Velocity vectors plotted on two-dimensional cross-sections of the simulation volume in Fig. 8 exhibits recirculation and flow impingement regions. Fig. 8(a) shows the distribution through the inlet duct ($z = 0.5233$ m). At downstream of the jet impingement, a major portion of the incoming fluid attaches the windshield upwards and creates a big recirculation with its eye in the middle of the plane. A smaller wake is also formed by the impingement filling the lower left corner of the plane. Fig. 8(b) shows noticeable difference in the vortex structure on the central plane ($z = 0.7233$ m) of the computational domain. The impinged fluid forms a bound vortex structure on this plane between the jets bending the fluid downward. The jets coming out of the defroster openings appear to the flow deflected by the windshield as "solid". A sharp velocity and temperature gradient is formed upstream of the jet while a "wake" region develops downstream of the jet. In the latter, a pair of bound vortices per jet is formed, which bends the jet both downward and upward, producing the well-known kidney shape in speed line contours.

Fig. 9 documents these bound vortices created between the jets on the vertical plane cutting through the inlet jet at $x = 0.144$ m. Flow deflected off the inclined surface and spreading throughout the simulation volume may form vortices of different size. Velocity vectors plotted in Fig. 10 on the horizontal plane cutting through $y = 0.2$ m shows multiple vortex structures. The air attached to the windshield is coming off the plane at the top of the plot. This complex three-dimensional nature of the fluid flow has significant influence on the heat transfer process between the jet and the inclined surface as well as inside the simulation volume.

The jet impingement process tremendously affects the temperature distribution on the windshield. Higher velocity near the wall causes a local cooling effect due to higher convective heat transfer. The near-wall fluid velocity vector distribution is shown in Fig. 11. Corresponding temperature contours on the inside surface of

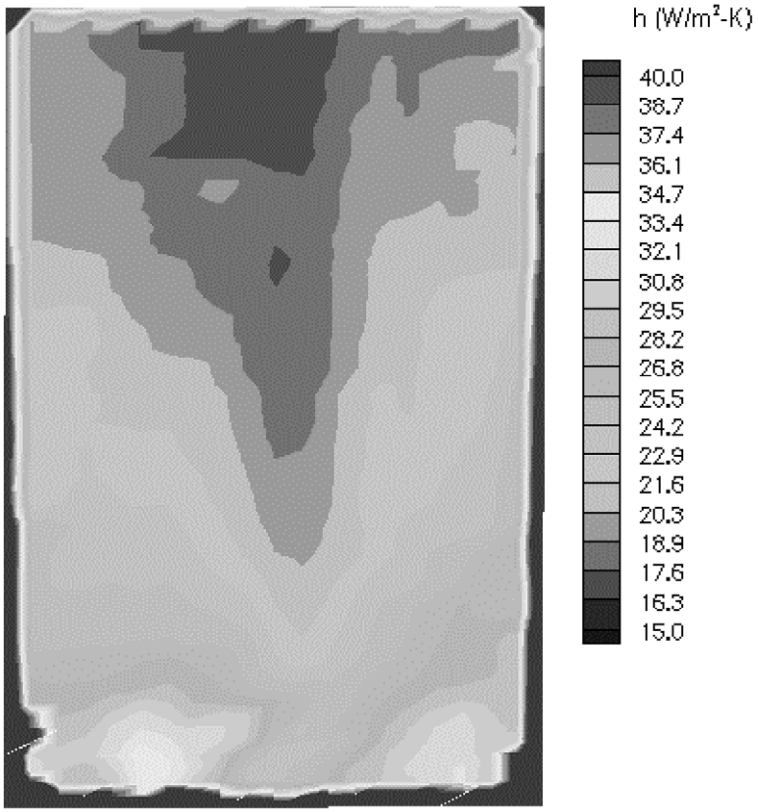

Fig. 13. Local convection heat transfer coefficient distribution on the inside surface of the windshield under the heating pad.

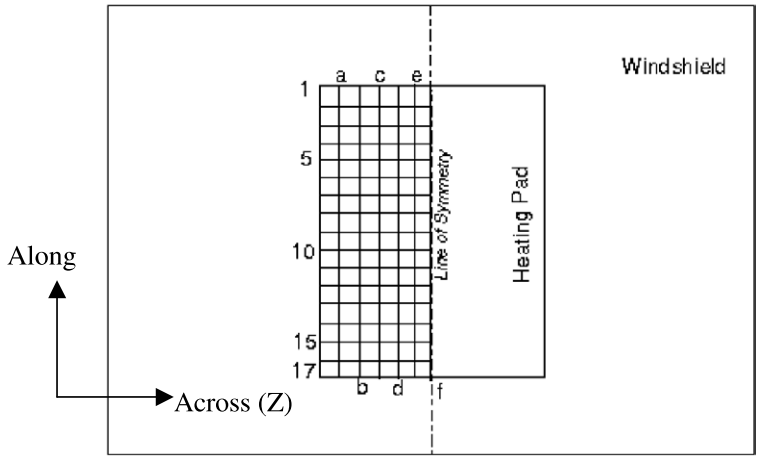

Points	Location along the Heating Pad* (m)
17	0.0254
16	0.0508
15	0.0762
14	0.1016
13	0.1270
12	0.1524
11	0.1778
10	0.2032
9	0.2286
8	0.2540
7	0.2794
6	0.3048
5	0.3302
4	0.3556
3	0.3810
2	0.4064
1	0.4318

Lines	Location across the Heating Pad (m)
f	Z= 0.7233
e	Z= 0.6849
d	Z= 0.6591
c	Z= 0.6333
b	Z= 0.6076
a	Z= 0.5819

Fig. 14. Locations of selected lines on the windshield (*measured from the bottom of the heating pad).

the windshield under the heated area in Fig. 12, shows an overall comparison between the experimental data (Fig. 4) and CFD prediction of thermal patterns. Note that the regions where the jets impinge upon the wall are about 7 (yellow) to 10 (green) degrees cooler than the top section (red) of the heating pad where much less heat is convected out. The predicted distribution of local convection heat transfer coefficient is plotted in Fig. 13, using (10), and shows the inverse relation between temperature and heat transfer coefficient h. The corresponding average heat transfer coefficient, calculated using (11) from the predicted results, is $\overline{h} = 27.35\ \mathrm{W/m^2\ K}$.

Even though Fig. 4, the experimentally based temperature contours, and Fig. 12, their numerical counterparts, display a reasonable match, the predicted temperature distribution on the inside of the heating pad should also be validated against the experimental data on a point-by-point basis. The selected locations for this validation are described on the inner surface of the windshield in Fig. 14. A detailed comparison of predicted and experimental temperature distribution done on 17 points on each of the six z-locations as displayed in Fig. 15, shows that the numerical prediction is within 1–5 °C of the measured data.

Finally, the Nusselt number (Nu) distribution on the heating pad along six z-locations (lines a–f in Fig. 14) is compared in Fig. 16 for three turbulence levels, $T_u = 0.1$, 0.05 and 0.02. Nusselt number is a function of local heat transfer coefficient, as the reference length and fluid

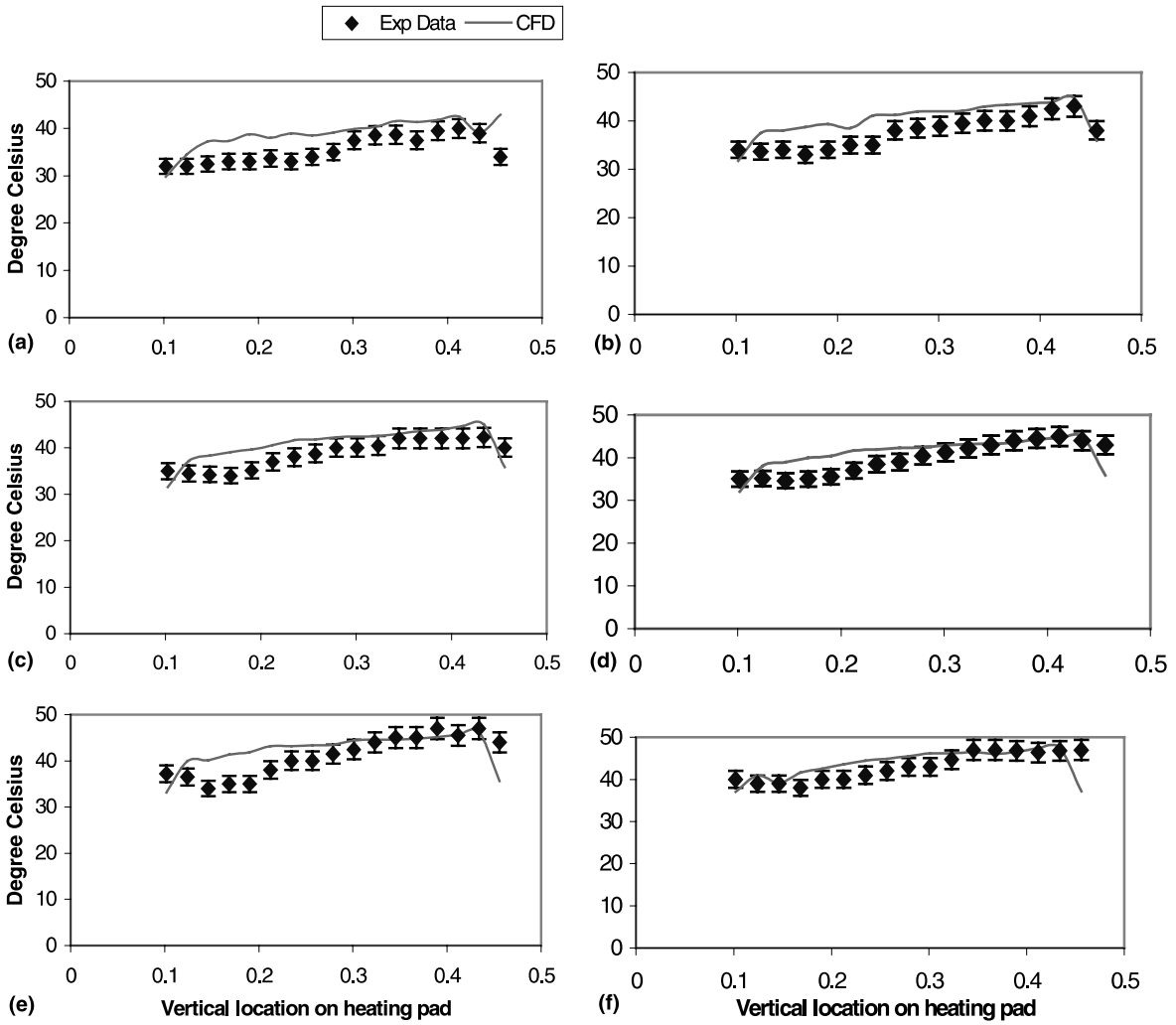

Fig. 15. Validation of CFD results with experimental data at different locations on the heating pad: (a) $z = 0.5819$ m; (b) $z = 0.6076$ m; (c) $z = 0.6333$ m; (d) $z = 0.6591$ m; (e) $z = 0.6849$ m; (f) $z = 0.7233$ m.

thermal conductivity remain constant. Thus its distribution gives better idea of jet impingement heat transfer modes through the surface. For this specific problem, the computed Nu varies negligibly (i.e., less than 1%) near the top of the heating pad except for the line of geometric symmetry ($z = 0.7233$ m) where $T_u = 0.02$ result is 10% higher than $T_u = 0.1$ result. However, the difference is quite large (4–11%) at the bottom of the pad for all plotted lines showing consistent overprediction by $T_u = 0.1$ in this region.

4. Conclusions

The paper addressed numerical and experimental studies of air jets impinging on an inclined surface. Experimental measurements of surface temperatures, using liquid crystals, yielded a map of local heat transfer coefficients between the surface and the incoming jet for an imposed heat flux. Corresponding three-dimensional numerical simulation has been performed using a finite-volume algorithm for obtaining detailed temperature and flow distributions. The numerical simulation correlated reasonably well with the experimental results and further explained the flow characteristics and thermal patterns. Despite some differences between the experimental setup and the computational model, a detail comparison on 102 locations inside the heating pad validated the numerical prediction within 1–5 °C of the observed values. It has thus been established that numerical simulation could be used to analyze practical problems with varying degrees of difficulty and feature

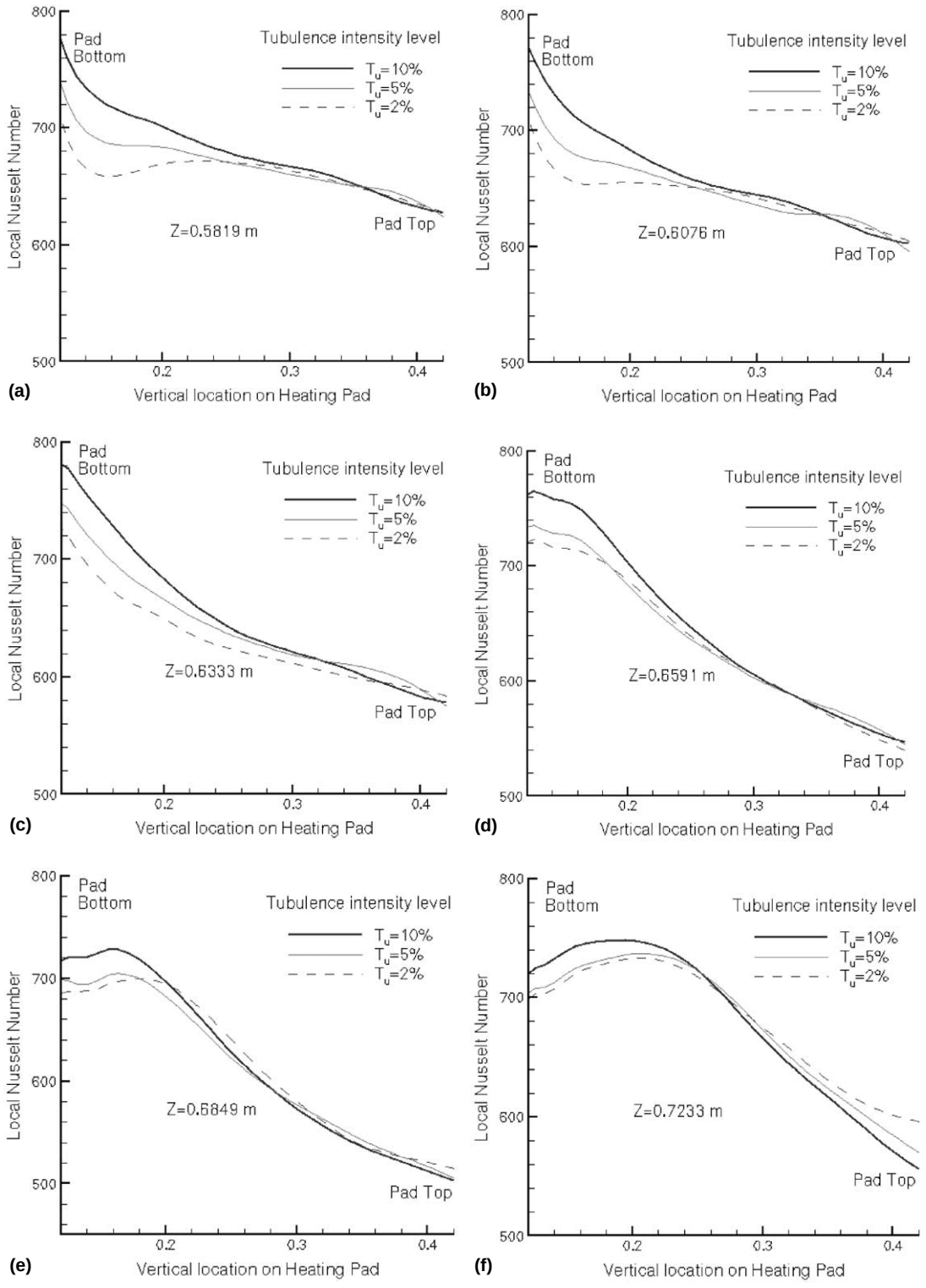

Fig. 16. Effect of inlet turbulence intensity level on the numerical heat transfer solution.

further flow and thermal characteristics. Documented *Nu* distributions on six specific lines on the heating pad shows the significance of adroit selection of turbulence level for the simulation. Further investigation should aim for the experimental quantification of heat transfer in the flow impingement region, wall jet, and recirculation zone.

Acknowledgements

This work was partially supported by NASA grant no NAG3-2520 with Maris Manteneiks as technical monitor.

References

[1] Y. Ishihara, M. Shibata, H. Hoshino, J. Hara, K. Kamemoto, Analysis of interior airflow in a full-scale passenger-compartment model using a laser-light-sheet method, 1992, SAE Paper 920206.
[2] L. Loefdahl, B. Johansson, C. Ljus, P. Alleving, A fast simple hot-wire method of determining the mean velocity vector of complex three-dimensional flows, Exp. Fluids 20 (1996) 398–400.
[3] M. Carignano, E. Pippione, Optimization of wind-screen defrosting for industrial vehicles via computer assisted thermographic analysis, 1990, FIJITA Paper 905237.
[4] L. Andreone, G. Burzio, S. Damiani, G. Romitelli, Automatic measurement of defrosting/defogging process, in: Proceedings of the 2nd International Conference on Vehicle Comfort Ergonomic, Vibrational, Noise, and Thermal Aspects, 1992, ATA Paper 92A272.
[5] K. Willenborg, J.F. Foss, R.S. AbdulNour, J.J. McGrath, B.S. AbdulNour, A model defroster flow, in: Proceedings of the Eleventh Symposium on Turbulent Shear Flows, vol. 2, 1997, pp. 15.25–15.30.
[6] R.S. AbdulNour, K. Willenborg, J.F. Foss, J.J. McGrath, B.S. AbdulNour, Measurements of the convective heat transfer coefficient for a two-dimensional wall jet: uniform temperature and uniform heat flux boundary conditions, in: M.E. Ulucakli, et al. (Eds.), Proceeding of ASME Heat Transfer Division, HTD 3, 1997, pp. 109–116.
[7] K.J. Nasr, B.S. AbdulNour, Defrosting of automotive windshields: progress and challenges, Int. J. Vehicle Des. 23 (3/4) (2000) 360–375.
[8] Y. Ikeda, N. Katoh, N. Ishii, T. Kuriyama, Numerical analysis of the airflow on windows from defroster nozzles, 1997, JSAE Paper 924076 (in Japanese).
[9] M. Sugano, T. Yamada, Y. Takesue, T. Yasuki, Numerical analysis of defroster cleaning pattern, 1994, JSAE Paper 9432912 (in Japanese).
[10] B.S. AbdulNour, J.F. Foss, Computational and experimental predictions of automotive windshield flow, in: Proceedings of ASME Fluids Engineering Division Summer Meeting, 1997, ASME Paper No. FEDSM97-3022.
[11] R. Brewster, S. Frick, F. Werner, Computational analysis of automotive windshield de-icing with comparison to test data, VTMS 3, 1997, Paper 971833.
[12] S. Polat, B. Huang, A.S. Mujumdar, W.J.M. Douglas, Numerical flow and heat transfer under impinging jets: a review, Ann. Rev. Numer. Fluid Mech. Heat Transfer 2 (1989) 157–197.
[13] J. Andreopoulos, W. Rodi, Experimental investigation of jets in a crossflow, J. Fluid Mech. 138 (1984) 93–127.
[14] H. Martin, Heat and mass transfer between impinging gas jets and solid surfaces, in: Advances in Heat Transfer, vol. 13, Academic Press, New York, 1977, pp. 1–60.
[15] S.J. Downs, E.H. James, Jet impingement heat transfer – a literature survey, 1987, ASME Paper No. 87-HT-35.
[16] R. Viskanta, Heat transfer to impinging isothermal gas and flame jets, Exp. Thermal Fluid Sci. 6 (1993) 111–134.
[17] J.C. Simonich, R.J. Moffat, New technique for mapping heat transfer coefficient contours, Rev. Sci. Instrum. 53 (5) (1982) 678–683.
[18] Hyperworks© 4.0 Online Users Manual, Altair Engineering, Troy, MI, 2000.
[19] FLUENT© 5 User's Guide, Fluent Inc., vols. 1–4, Lebanon, NH, 1998.
[20] H. Johari, M. Pacheco-Tougas, J.C. Hermanson, Penetration and mixing of fully modulated turbulent jets in crossflow, AIAA J. 37 (1999) 842–850.
[21] S. Roy, Numerical investigation of the blade cooling effect generated by multiple jets issuing at an angle into an incompressible horizontal cross flow, Numer. Heat Transfer A 38 (7) (2000) 701–718.
[22] V. Yakhot, S.A. Orszag, Renormalization group analysis of turbulence. I. Basic theory, J. Sci. Comput. 1 (1986) 3–51.
[23] S.H. Lam, On the RNG theory of turbulence, Phys. Fluids A 4 (1992) 1007–1017.
[24] R.J. Moffat, Describing the uncertainties in experimental results, Exp. Thermal Fluid Sci. 1 (1988) 3–17.